Modern Approaches to Plasticity / D. Kolymbas (Editor)

Simple and Generalized Modelling of Various Soil Behaviour in Three-Dimensional Stresses

T. Nakai, H. Taki, T. Funada

1 Introduction

In constitutive models for sand which are applicable to practical problems, the following points should be taken into consideration :

1 Influence of intermediate principal stress on the deformation and strength of sand,

2 Stress path dependency of flow rule,

3 Positive and negative dilatancy,

4 Induced anisotropy by stress history such as cyclic loading, rotation of principal stress axes and others,

5 Inherent anisotropy formed during deposition process or sample preparation.

An isotropic hardening model (named t_{ij}-sand model) which describes the above points 1 to 3 properly is firstly presented (Nakai, 1989). This isotropic hardening model is extended to a kinematic hardening model (named kinematic t_{ij}-sand model) that successfully describes the point 4 as well as the points 1 to 3 (Nakai, Fujii and Taki, 1989). Furthermore, this kinematic hardening model is extended to a model which takes into consideration not only points 1 to 4 but also inherent anisotropy (point 5) by introducing a fabric anisotropy tensor b_{ij} (Nakai and Funada, 1992).

2 Stress Parameters Used in t_{ij}-Concept

Before the formulation of models for sand, we will describe briefly the stress parameters based on the t_{ij}-concept and the method of applying this concept to elastoplastic modelling. Through the t_{ij}-concept, the influence of

intermediate principal stress is successfully modelled. Table 1 shows the comparison of various tensors and scalars related to stress between ordinary concept and t_{ij}-concept. Equations (1a) to (5a) and (7a) are the well-known scalars and tensors used in most models such as the Cambridge model. Figure 1 shows these quantities in σ_{ij}-space. Equations (6a) and (8a) are the quantities introduced by Sekiguchi and Ohta (1977) so as to extend the Cambridge model (Schofield and Wroth, 1968) to one in which initial stress induced anisotropy can be taken into consideration.

In the t_{ij}-concept, we firstly introduce a tensor a_{ij}, which is a symmetric tensor whose principal values are determined by the direction cosines of spatially mobilized plane (briefly SMP) (Matsuoka and Nakai, 1974) and is expressed as follows using the stress tensor (Nakai, 1989):

$$a_{ij} = \sqrt{\frac{J_3}{J_2}} r_{ij}^{-1} = \sqrt{\frac{J_3}{J_2}} (\sigma_{ik} + I_2 \delta_{ik})(I_1 \sigma_{kj} + I_3 \delta_{kj})^{-1} \tag{1}$$

where J_2 and J_3 are the second and third stress invariants, and I_1, I_2 and I_3 are the first, second and third invariants of r_{ij}, which is the stress tensor σ_{ij} to the one-half power such as $r_{ik} r_{kj} = \sigma_{ij}$. It can be seen from the above equation that the variable a_{ij} is a function of stress ratio. The modified stress tensor t_{ij} is then defined by Eq. (1b) as the product of σ_{ik} and a_{kj}. Employing t_{ij} and a_{ij} of Eqs. (1b) and (2b) in place of σ_{ij} and δ_{ij} of Eqs. (1a) and (2a), we can obtain analogically the scalar and tensors used in the t_{ij}-concept as Eqs. (3b) to (8b). Figure 2 shows these quantities in the t_{ij}-space. Now, the influence of intermediate principal stress is naturally taken into consideration by employing the quantities of Eqs. (1b) to (8b) in place of those of Eqs. (1a) to (8a) and assuming the flow rule not in σ_{ij}-space but in t_{ij}-space (Nakai and Mihara, 1984; Nakai, 1989).

3 Isotropic Hardening Model for Sand (t_{ij}-Sand Model)

3.1 Outline of Model

Since details of the model are described in another paper (Nakai, 1989), only the outline is presented here. The total strain increment $d\varepsilon_{ij}$ is given by the summation of the elastic component $d\varepsilon_{ij}^{e}$, the plastic component $d\varepsilon_{ij}^{p(AF)}$ which satisfies the associated flow rule in t_{ij}-space and the plastic component $d\varepsilon_{ij}^{p(IC)}$ which represents isotropic compression.

ordinary concept		t_{ij}-concept	
σ_{ij}	(1a)	$t_{ij} = \sigma_{ik}a_{kj}$	(1b)
δ_{ij} (unit tensor)	(2a)	a_{ij}	(2b)
$p = \sigma_{ij}\delta_{ij}/3$	(3a)	$t_N = t_{ij}a_{ij}$	(3b)
$s_{ij} = \sigma_{ij} - p\delta_{ij}$	(4a)	$t'_{ij} = t_{ij} - t_N a_{ij}$	(4b)
$q = \sqrt{(3/2)s_{ij}s_{ij}}$	(5a)	$t_S = \sqrt{t'_{ij}t'_{ij}}$	(5b)
$\eta_{ij} = s_{ij}/p$	(6a)	$x_{ij} = t'_{ij}/t_N$	(6b)
$\eta \equiv q/p = \sqrt{(3/2)\eta_{ij}\eta_{ij}}$	(7a)	$x \equiv t_S/t_N = \sqrt{x_{ij}x_{ij}}$	(7b)
$\eta^* = \sqrt{(3/2)(\eta_{ij} - \eta_{ij0})(\eta_{ij} - \eta_{ij0})}$	(8a)	$x^* = \sqrt{(x_{ij} - n_{ij})(x_{ij} - n_{ij})}$	(8b)

TABLE 1. Comparisons of various tensors and scalars related to stress between ordinary concept and t_{ij}-concept

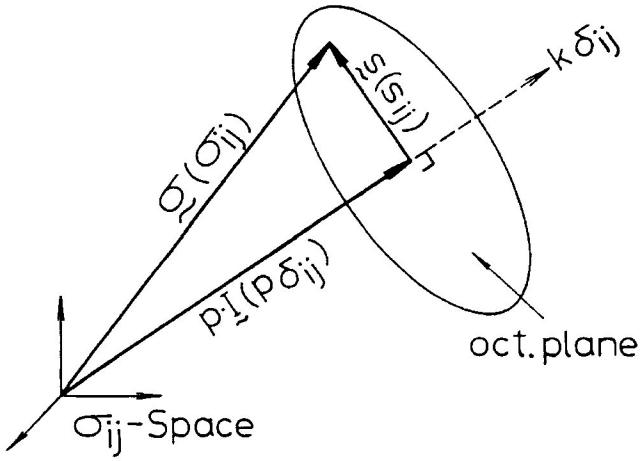

FIGURE 1. Illustration of stress quantities in σ_{ij}-space which are used in the ordinary concept

$$d\varepsilon_{ij} = d\varepsilon^e_{ij} + d\varepsilon^p_{ij} = d\varepsilon^e_{ij} + d\varepsilon^{p(AF)}_{ij} + d\varepsilon^{p(IC)}_{ij} \tag{2}$$

The three components are calculated according to the following expression:

$$d\varepsilon_{ij} = \frac{1+\nu_e}{E_e}d\sigma_{ij} - \frac{\nu_e}{E_e}d\sigma_{kk}\delta_{ij} \tag{3}$$

$$d\varepsilon^{p(AF)}_{ij} = \Lambda\frac{\partial f}{\partial t_{ij}} \tag{4}$$

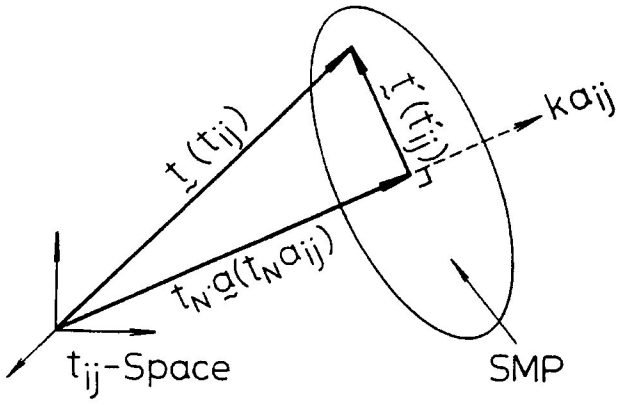

FIGURE 2. Illustration of stress quantities in t_{ij}-space which are used in t_{ij} concept

$$d\varepsilon_{ij}^{p(IC)} = K\langle dp\rangle \frac{\delta_{ij}}{3} \tag{5}$$

Here, f is the yield function, and the bracket $\langle dp\rangle$ implies $\langle dp\rangle = dp$ if $dp > 0$ and $df > 0$; otherwise $\langle dp\rangle = 0$. Young's modulus E_e and the coefficient K are expressed as

$$E_e = 3(1-2\nu_e)P_a^m/(m\,C_e\,p^{m-1}) \tag{6}$$

$$K = m(C_t - C_e)\frac{p^{m-1}}{P_a^m} \qquad (P_a : \text{atmospheric pressure}) \tag{7}$$

Equations (6) and (7) can be derived from the relationship for the elastic and plastic volumetric strains and mean stress under isotropic compression such as

$$(\varepsilon_v^e)_{iso} = C_e\left\{\left(\frac{p}{P_a}\right)^m - \left(\frac{p_0}{P_a}\right)^m\right\} \tag{8}$$

$$(\varepsilon_v^p)_{iso} = (C_t - C_e)\left\{\left(\frac{p}{P_a}\right)^m - \left(\frac{p_0}{P_a}\right)^m\right\} \tag{9}$$

The yield function f is given by

$$f = \ln t_N - \frac{\alpha}{1-\alpha} \ln |1 - (1-\alpha)\frac{X}{M^*}| - c = 0 \tag{10}$$

where

$$M^* = X_f + \alpha Y_f \tag{11}$$

Further, X_f and Y_f are given using the principal stress ratio $R_f \equiv (\sigma_1/\sigma_3)_{f(comp.)}$ and strain increment ratio $D_f \equiv (d\varepsilon_v/d\varepsilon_1)_{f(comp.)}$ at failure in a conventional triaxial compression test (Nakai, 1989).

$$X_f = \frac{\sqrt{2}}{3}\left(\sqrt{R_f} - \sqrt{\frac{1}{R_f}}\right) \tag{12}$$

$$Y_f = \frac{1 - \sqrt{R_f}(1 - D_f)}{\sqrt{2}\{\sqrt{R_f} + 0.5(1 - D_f)\}} \tag{13}$$

The scalar Λ in Eq. (4) is determined as follows utilising that "the plastic work based on t_{ij}", $W^{*p} = \int t_{ij} d\varepsilon^p_{ij}$, is a quantity of state for sand under monotonic loading:

$$\Lambda = \frac{dW^{*p} - K\langle dp\rangle \frac{\delta_{ij}}{3} t_{ij}}{\frac{\partial f}{\partial t_{kl}} t_{kl}} \tag{14}$$

where dW^{*p} is

$$\begin{aligned} dW^{*p} &= \frac{\partial W^{*p}}{\partial t_N} dt_N + \frac{\partial W^{*p}}{\partial X} dX \\ &= \frac{m(C_t - C_e) t_N^{m+1}}{\sqrt{3} P_a^m} \left\{1 - (1-\alpha)\frac{X}{M^*}\right\}^{\frac{-\alpha(m+1)}{1-\alpha}} \\ &\quad \times \left\{\frac{1}{t_N} dt_N + \frac{\alpha}{M^* - (1-\alpha)X} dX\right\} \end{aligned} \tag{15}$$

In this model, the influence of intermediate principal stress on the deformation and strength of sand is taken into consideration by using the t_{ij}-concept as described in the previous section, the stress path dependency of flow rule by dividing plastic strain increment into two components (see Eq. 2) and the positive and negative dilatancy by employing $W^{*p} = \int t_{ij} d\varepsilon^p_{ij}$ as a strain hardening parameter.

C_t	$0.84 \cdot 10^{-2}$
C_e	$0.60 \cdot 10^{-2}$
m	0.3
$R_f = (\sigma_1/\sigma_3)_{f(comp.)}$	4.7
$D_f = (\mathrm{d}\varepsilon_v/\mathrm{d}\varepsilon_1)_{f(\mathrm{comp.})}$	-0.6
α	0.85

TABLE 2. Values of soil parameters for Toyoura sand used in analysis

3.2 VERIFICATION BY TEST RESULTS

Table 2 shows the values of soil parameters of medium dense Toyoura sand ($e_0 \simeq 0.68$). The values of C_t, C_e and m are determined from a loading and unloading isotropic compression test. The parameters R_f and D_f stand for the principal stress ratio $(\sigma_1/\sigma_3)_f$ and the strain increment ratio $(d\varepsilon_v/d\varepsilon_1)_f$ at failure under triaxial compression, and α also is related to the strain at failure. So, the values of Table 2 can be determined from a test under the stress path in Fig. 3.

Figure 4 shows the observed values (dots) and calculated stress-strain curves of triaxial compression and triaxial extension tests under constant minor principal stress, constant mean principal stress and constant major principal stress. The model describes well not only the difference between triaxial compression and triaxial extension but also the difference of stress-strain curves and dilatancy due to stress path.

Figure 5 shows the observed values (dots) and calculated curves of monotonic loading true triaxial tests under constant mean principal stress, arranged in terms of the relation between principal stress ratio and principal strains. Figure 6 shows the observed and calculated directions of the strain increments on the octahedral plane in these true triaxial tests. The model predicts well the three dimensional stress strain behaviour of sand, inclusive deviation of shear strain increment direction from that of the shear stress.

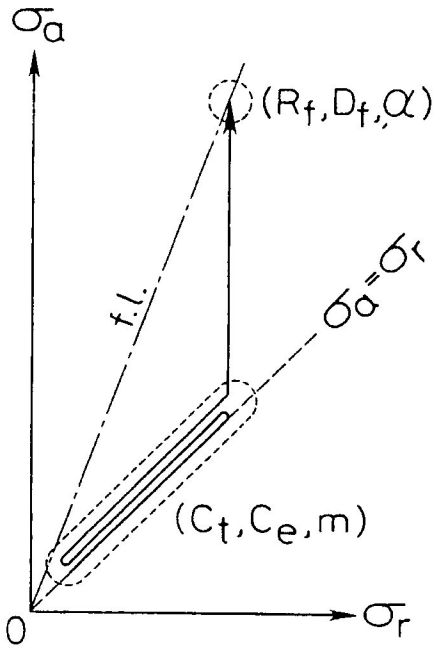

FIGURE 3. Stress path of test to determine values of soil parameters

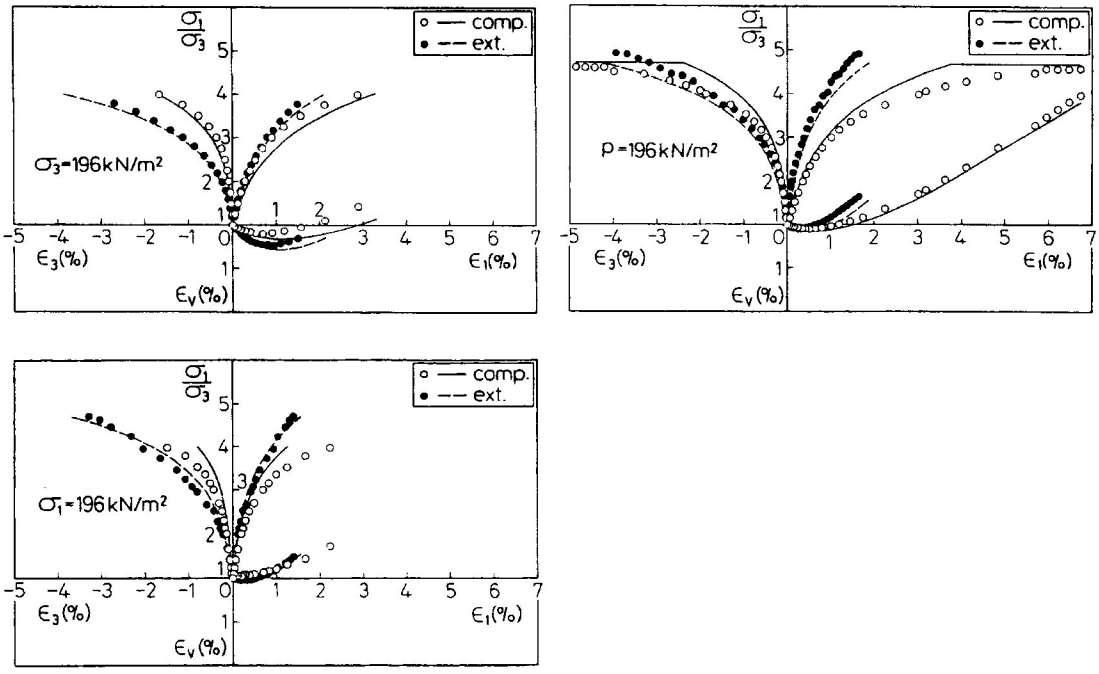

FIGURE 4. Principal strains vs. principal stress ratio and volumetric strain in triaxial compression and extension tests, (a) constant minor principal stress tests, (b) constant mean principal stress tests, (c) constant major principal stress tests

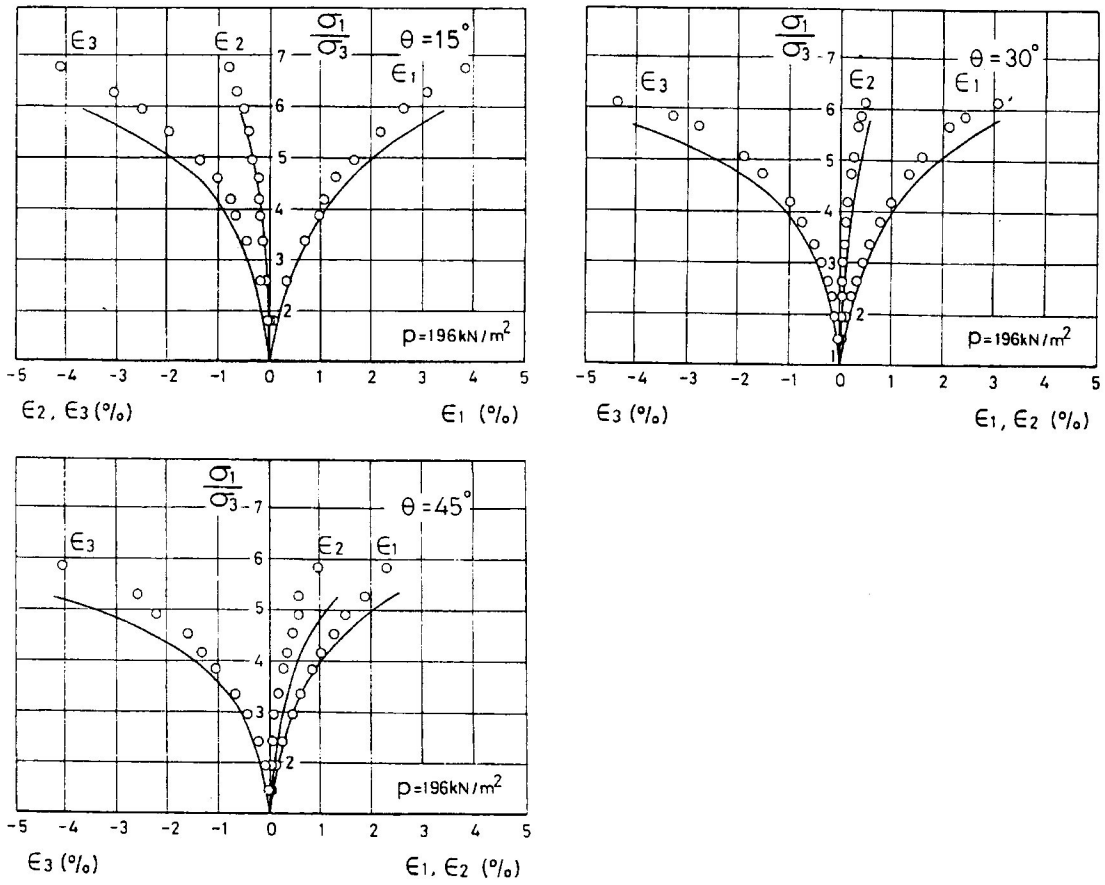

FIGURE 5. Principal strains vs. principal stress ratio in true triaxial tests, (a) $\theta = 15°$, (b) $\theta = 30°$, (c) $\theta = 45°$

4 Kinematic Hardening Model for Sand (Kinematic t_{ij}-Sand Model)

4.1 Extension from isotropic hardening model to kinematic hardening model

In order to extend the above isotropic hardening model into one which obeys the kinematic hardening rule on the shear behaviour, we introduce the stress ratio tensor x_{ij} in Eq. (6b) and the scalar quantity of stress ratio X^* in Eq. (8b) in Table 1. Since under monotonic loading paths in triaxial compression and extension conditions the following equation holds

$$X := X^* + n \qquad (\text{where } n = \sqrt{n_{ij} n_{ij}}) \tag{16}$$

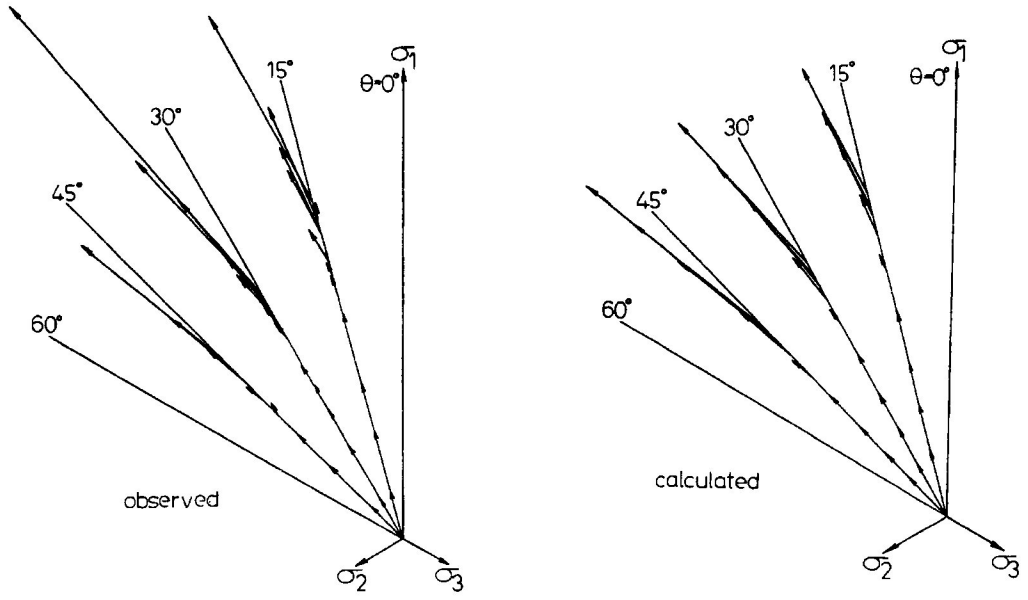

FIGURE 6. Stress paths and strain increment vectors on octahedral plane in true triaxial tests (a) observed, (b) calculated

we replace the stress ratio X in Eq. (10) by $X^* + n$ and give the yield function by

$$f = \ln t_N - \frac{\alpha}{1-\alpha} \ln \left| 1 - (1-\alpha) \frac{X^* + n}{M^*} \right| - c = 0 \tag{17}$$

As known from Sekiguchi and Ohta model (1977) using Eqs. (6a) and (8a), such formulation makes possible to take into consideration the stress ratio history and rotation of principal axes. Now, though in Sekiguchi and Ohta model the tensor η_{ij0} in Eq. (8a) is determined from the stress state before loading and is not varying, we assume in the present model that the tensor n_{ij} in Eq. (8b) is movable with satisfying the following condition.

$$X^* = \sqrt{(x_{ij} - n_{ij})(x_{ij} - n_{ij})} = \xi \quad (= \text{const.}) \tag{18}$$

Figure 7 shows the relation of the position between the current stress ratio tensor x_{ij} on the yield surface and the tensor n_{ij} in the stress ratio space x_{ij}. When such a stress ratio increment dx_{ij} as shown in Fig. 7 is applied, n_{ij} is assumed to move to the direction of $(x_{ij} - n_{ij})$ with keeping the distance ξ. The following equations, hence, hold:

$$dn_{ij} = k(x_{ij} - n_{ij}) \tag{19}$$

$$dX^* = \frac{\partial X^*}{\partial x_{ij}} dx_{ij} + \frac{\partial X^*}{\partial n_{ij}} dn_{ij} = 0 \tag{20}$$

From Eqs. (19) and (20), the increment dn_{ij} follows as

$$\mathrm{d}n_{ij} = \frac{(x_{kl} - n_{kl})\mathrm{d}x_{kl}}{X^{*2}}(x_{ij} - n_{ij}) \tag{21}$$

The position of n_{ij} corresponding to the change in x_{ij} is successively obtained by Eq. (21) so that the direction of plastic flow of $d\varepsilon_{ij}^{p(AF)}$ is determined using Eq. (17) and the associated flow rule in t_{ij}-space (Eq. 4). Here, when under the condition of $X^* < \xi$ a plastic strain increment occurs ($f = 0$ and $\mathrm{d}f > 0$), we presume that the yield surface expands without change in n_{ij} like isotropic hardening model until X^* becomes ξ.

Figure 8 illustrates the yield surfaces of t_{ij}-sand model and kinematic t_{ij}-sand model in $t_N - t_S$ space under the stress condition of triaxial compression. The shape of yield surface of isotropic hardening model is always symmetric with respect to t_N axis, whereas that of kinematic hardening model inclines upward. However, both of the yield surfaces are common in compression side so that the directions of plastic flow calculated by both models are the same under monotonic loading stress path such as triaxial compression. Figure 9 also shows schematically the change of yield surface in $t_N - t_S$ space under shear loading and proportional loading. The yield surface rotates about the origin under shear loading, because a kinematic hardening rule is assumed in the stress ratio space. On the other hand, the yield surface expands isotropically or anisotropically under proportional loading in the same way as the Cambridge model and the Sekiguchi and Ohta model.

Next, we will discuss the hardening function. The scalar value Λ in Eq. (4) is determined so as to describe the same stress-strain relationship as those in the isotropic hardening model under monotonic loading. Now, the increment dW^{*p} in Eq. (15) is given by invariants of stress and stress increment alone, i.e. t_N, dt_N, X and dX. Because the kinematic hardening model obeys the kinematic hardening rule only in shear behaviour (change in stress ratio), we introduce the stress ratio $\overline{\overline{X}}$ and a stress ratio increment $\overline{\overline{\mathrm{d}X}}$ in place of X and dX (see Fig. 10):

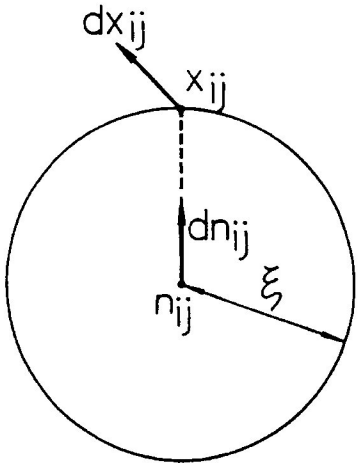

FIGURE 7. Kinematic hardening rule in stress ratio space (x_{ij})

$$\overline{\overline{X}} = X\cos\theta = \frac{x_{ij}\,x^*_{ij}}{X^*} \quad , \tag{22}$$

$$\overline{\overline{\mathrm{d}X}} = \mathrm{d}X\cos\theta = \frac{\mathrm{d}x_{ij}\,x^*_{ij}}{X^*} \quad , \tag{23}$$

where $x^*_{ij} = x_{ij} - n_{ij}$, and obtain the following equation:

$$dW^{*p} = \frac{m(C_t - C_e)t_N^{m+1}}{\sqrt{3}P_a^m}\left\{1-(1-\alpha)\frac{\overline{\overline{X}}}{M^*}\right\}^{\frac{-\alpha(m+1)}{1-\alpha}} \times\left\{\frac{1}{t_N}\mathrm{d}t_N + \frac{\alpha}{M^*-(1-\alpha)\overline{\overline{X}}}\overline{\overline{\mathrm{d}X}}\right\} \tag{24}$$

Since $\overline{\overline{X}}$ and $\overline{\overline{\mathrm{d}X}}$ vary with stress even when the stress invariants are constant, we can determine the scalar value of Λ in kinematic hardening model by employing dW^{*p} in Eq. (24). It is also noticed that $\overline{\overline{X}}$ and $\overline{\overline{\mathrm{d}X}}$ coincide with X and $\mathrm{d}X$ respectively under such monotonic loading paths as triaxial compression and extension.

The isotropic hardening model is extended to one in which the stress induced anisotropy can be taken into consideration only by introducing a stress ratio X^* and assuming a kinematic hardening rule in the stress ratio space x_{ij}.

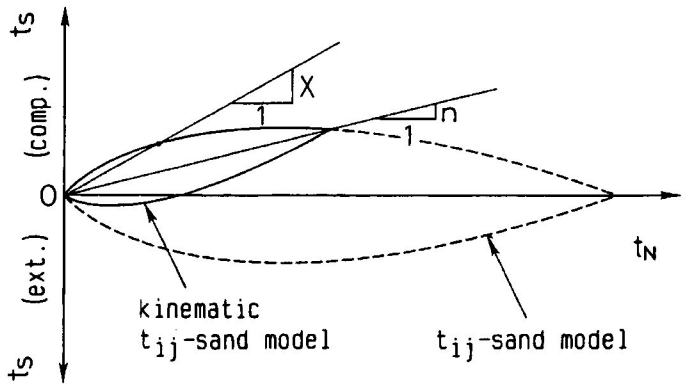

FIGURE 8. Yield surfaces of isotropic and kinematic hardening models in $t_N - t_S$ space

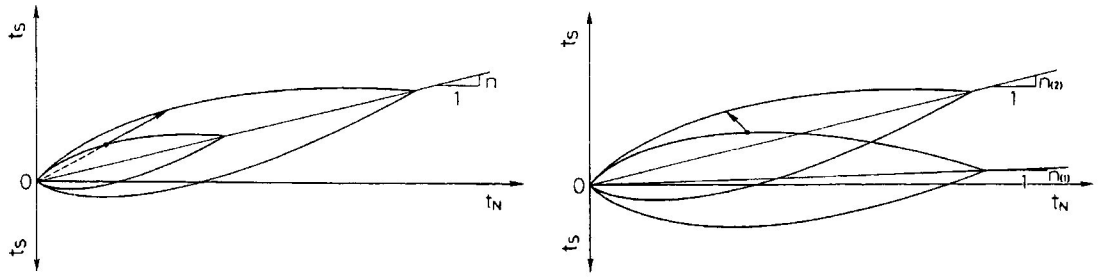

FIGURE 9. Evolution of yield surface of kinematic hardening model represented in $t_N - t_S$ space (a)under shear loading, (b)under proportional loading

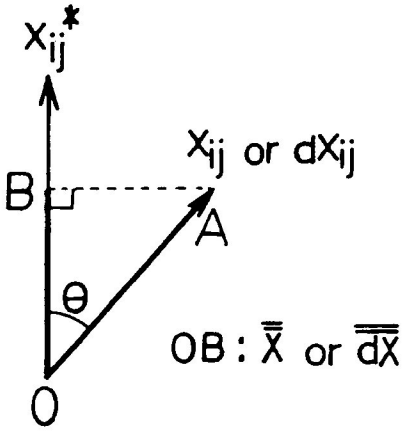

FIGURE 10. Definition of $\overline{\overline{X}}$ and $\overline{\overline{dX}}$ in x_{ij} space

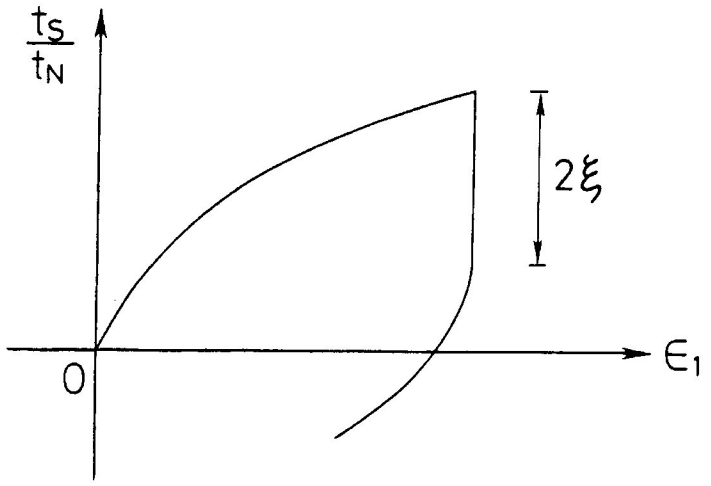

FIGURE 11. Methods to determine the value of ξ

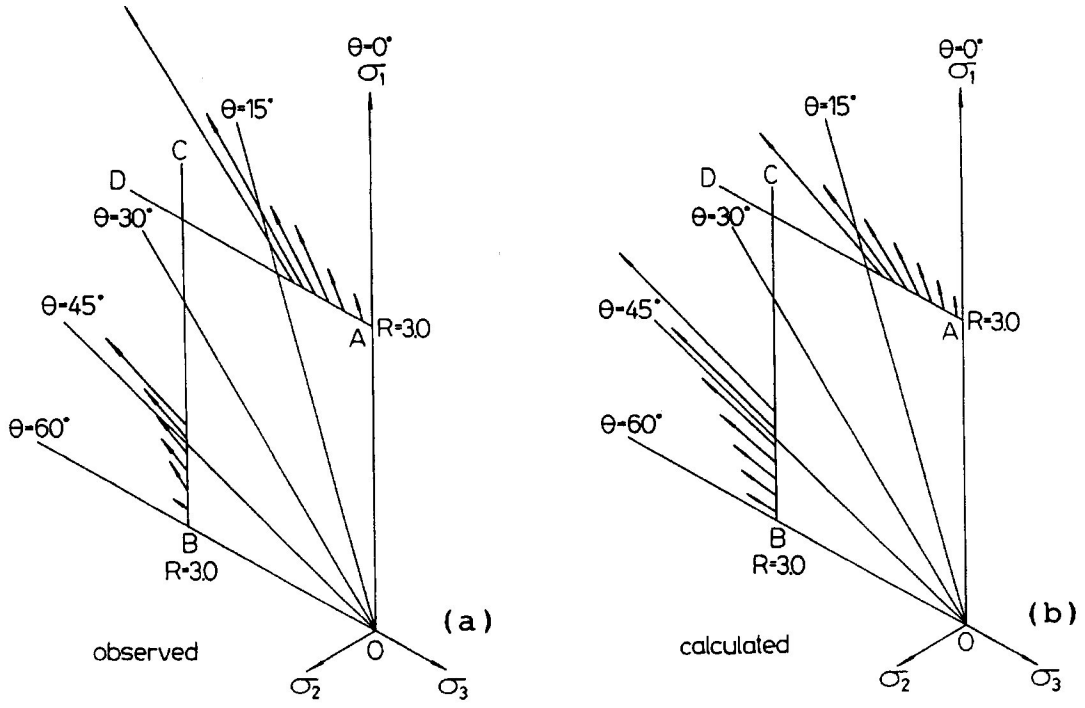

FIGURE 12. Stress paths and strain increment vectors on octahedral plane in path AD and BC, (a) observed, (b) calculated

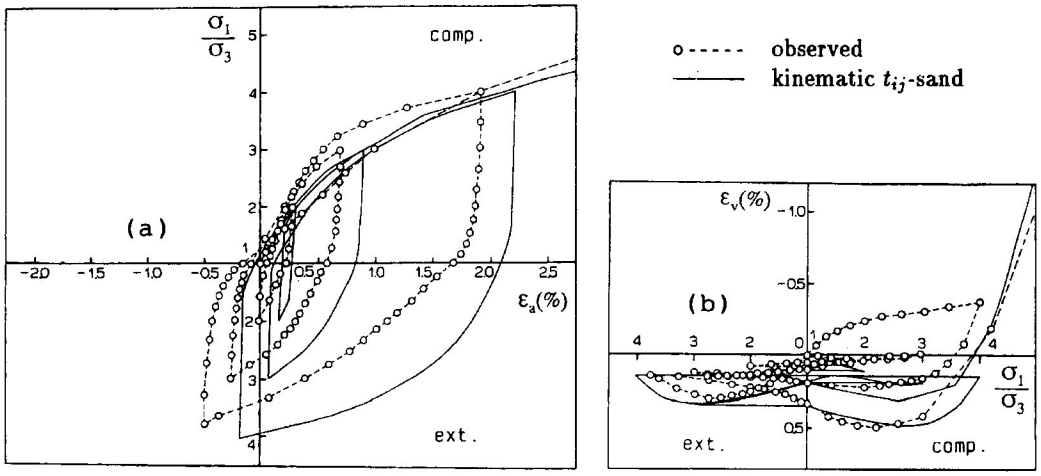

FIGURE 13. Stress-strain relation in cyclic triaxial test under constant mean principal stress, (a) axial strain vs. principal stress ratio, (b) principal stress ratio vs. volumetric strain

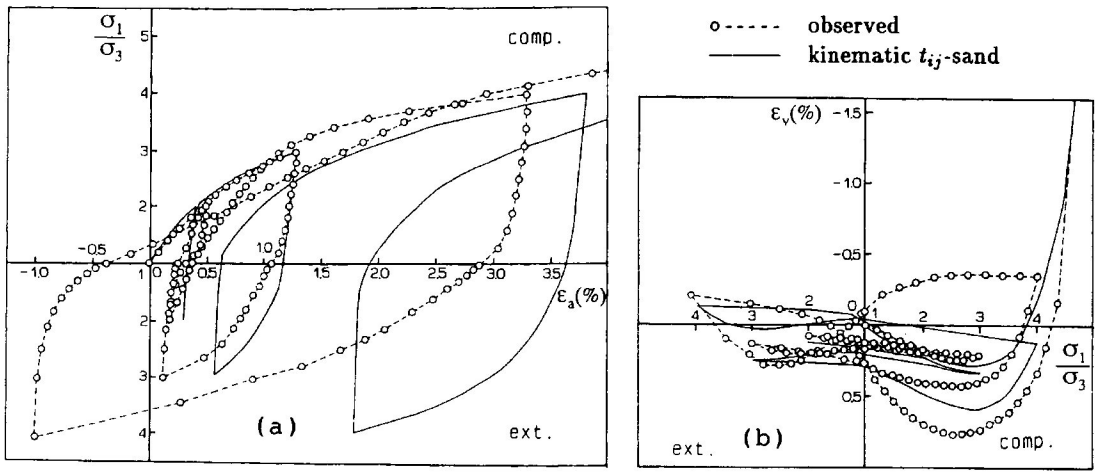

FIGURE 14. Stress-strain relation in cyclic triaxial test under constant minor principal stress, (a) axial strain vs. principal stress ratio, (b) principal stress ratio vs. volumetric strain

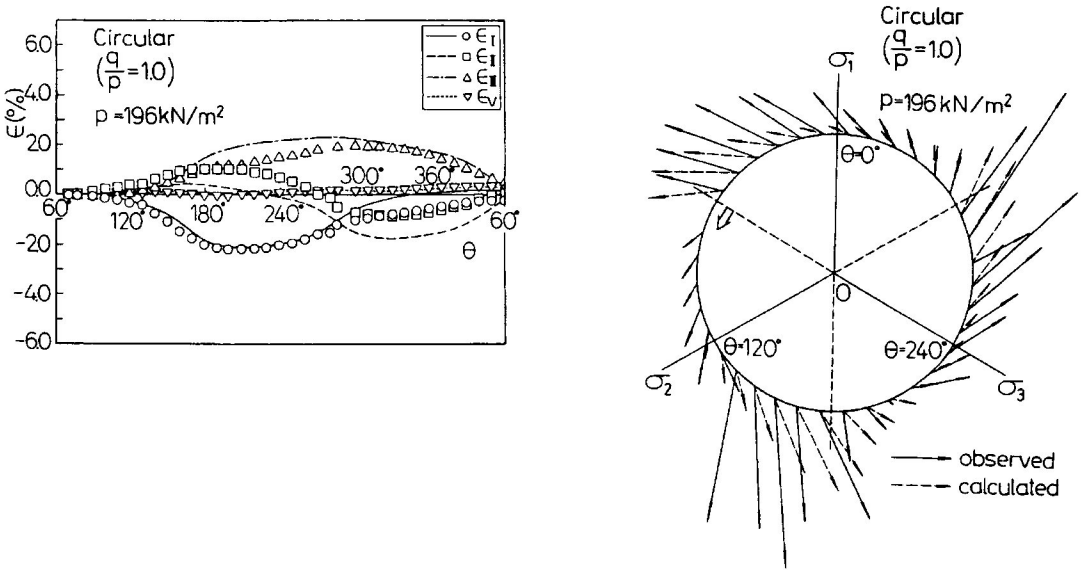

FIGURE 15. Experimental and analytical results of circular stress path test on octahedral plane, (a) variation of principal strains and volumetric strain, (b) stress path and strain increment vectors on octahedral plane

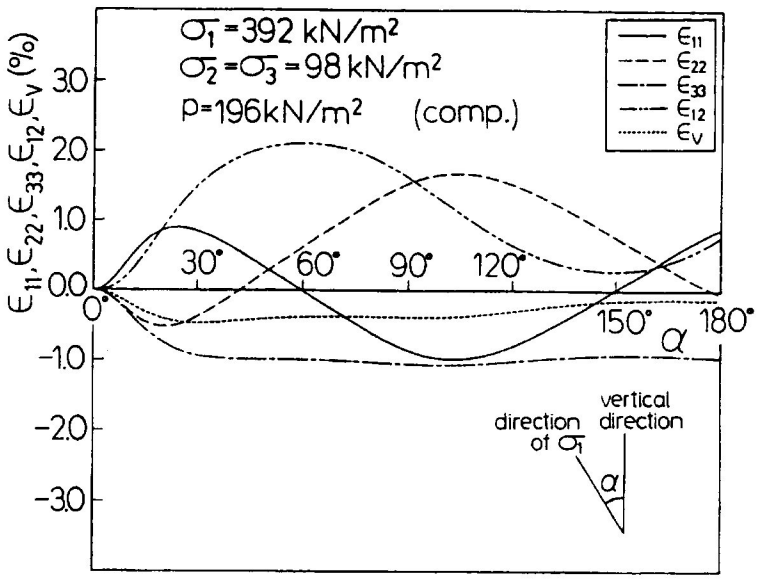

FIGURE 16. Calculated variation of various strains under rotation of principal stress axes

4.2 VERIFICATION BY TEST RESULTS

The soil parameter added in the kinematic hardening model is ξ alone, which represents the size of yield surface in the stress ratio x_{ij}-space. This can be determined from the elastic region under reversed shear loading, because the elastic region (range of stress ratio $X \equiv t_S/t_N$) corresponds to 2ξ as shown in Fig. 11. For medium dense Toyoura sand the value of ξ is determined as $\xi = 0.3$. The other parameters are the same as those of Table 2.

Figure 12 shows the stress paths and the observed and calculated directions of the shear strain increments on the octahedral plane in true triaxial tests, where the principal stress ratios are $R \equiv \sigma_1/\sigma_3 = 3.0$ at A and B. It has been known that in radial shear tests under three different principal stresses (e.g. $\theta = 15°, 30°$ and $45°$) the directions of shear strain increments deviate leftward (towards the extension side) from those of shear stresses (radial directions) with increase in stress ratio (see Fig. 6). Such a tendency, however, is not necessarily observed in the paths AD and BC (e.g. see near the intersection of $\theta = 45°$ line and path BC of figure (a)). This difference results in the influence of the stress path history. We can see from figure (b) that this influence is properly taken into consideration in the present model.

Figures 13 and 14 show the observed values (dots) and the analytical stress-strain curves of cyclic triaxial tests (Figure 13 is under constant mean principal stress, and Figure 14 is under constant minor principal stress). The kinematic hardening model predicts well the behaviour of sand under cyclic loading.

Figure 15(a) shows the observed and the calculated variation of the three principal strains and of the volumetric strain under a circular stress path ($\eta \equiv q/p = 1.0$) on octahedral plane. Figure 15(b) shows the observed and the calculated direction of the shear strain increments on the octahedral plane, together with the stress path. The stress path is rounded anticlockwise from $\theta = 60°$ to $\theta = 60°$. We can see from these figure that the model describes well the behaviour of sand under rotational stress path in three-dimensional stress too.

Figure 16 shows the analytical results of strains when only the principal stress axes rotates with keeping all of the stress invariants constant. Here, the stress condition is always under triaxial compression of $\sigma_1/\sigma_3 = 4.0$ and $p = 196\ \mathrm{kN/m^2}$. The horizontal axis α denotes the angle between vertical direction (direction of initial major principal stress) and the direction of major principal stress in every moment. This analytical result agrees qualitatively

with the results reported before.

5 Kinematic Hardening Model for Sand with Anisotropy (Kinematic t_{ij}-Sand (Anisotropic) Model)

5.1 Extension from model for isotropic sand to model for anisotropic sand

Even the kinematic hardening model described in the previous section cannot take into consideration inherent anisotropy which is formed during the deposition process or during the sample preparation. It is known that induced anisotropy changes with stress state and does not considerably affect the strength represented by effective stress (effective internal friction angle). On the other hand, the degree of inherent anisotropy does not change even if stress changes, and the strength as well as the deformation is influenced by the inherent anisotropy. In this section, a method to take into consideration the inherent anisotropy in constitutive models for sand is described. For this purpose, the stress ratio tensor x_{ij} is modified by a fabric anisotropy tensor b_{ij}; X^* in Eq. (17) is replaced by $\overline{X}^*$ as follows:

$$f = \ln t_N - \frac{\alpha}{1-\alpha} \ln \left| 1 - (1-\alpha) \frac{\overline{X}^* + n}{M^*} \right| - c = 0 \tag{25}$$

where $\overline{X}^*$ is expressed as

$$\overline{X}^* = \sqrt{(\overline{x}_{ij} - n_{ij})(\overline{x}_{ij} - n_{ij})} \tag{26}$$

and $\overline{x}_{ij}$ is defined by the following equation using fabric anisotropy tensor b_{ij}

$$\overline{x}_{ij} = \frac{1}{2} \frac{(t_{ik} b_{kj} + b_{ik} t_{kj})}{t_N} - a_{ij} \tag{27}$$

The fabric anisotropy tensor b_{ij} is a symmetric tensor whose trace is 3 ($b_{ii} = 3$). Furthermore, if $b_{ij} = \delta_{ij}$ (unit tensor), $\overline{x}_{ij}$ (Eq. 27) is identical to x_{ij} (Eq. 6b) in Table 1. The yield function f of Eq. 25 moves kinematically in the stress ratio tensor space ($\overline{x}_{ij}$-space) with the distance $\overline{X}^*$ equal to ξ for a change in $\overline{x}_{ij}$, and expands isotropically for a change in mean stress t_N in the same way as that for isotropic sand.

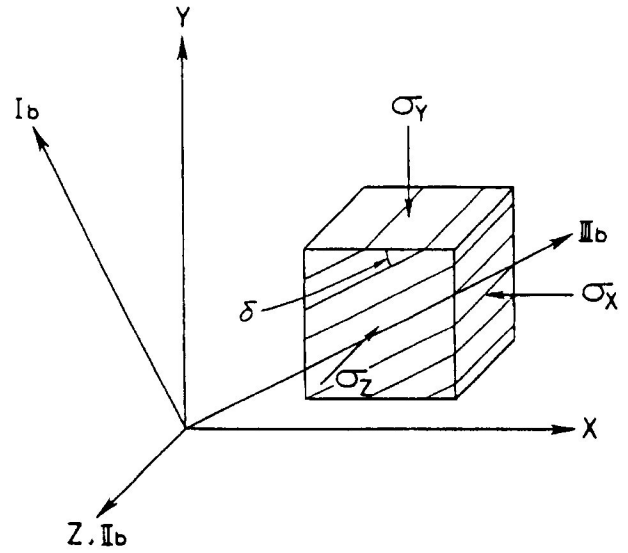

FIGURE 17. Principal axes (I_b, II_b and III_b) of fabric anisotropy tensor and angle δ between bedding plane and major principal stress plane

The quantities $\overline{\overline{X}}$ and $\overline{\overline{dX}}$ in Eq. 24 are also given by the projection of $\overline{x}_{ij}$ and $\mathrm{d}\overline{x}_{ij}$ in the direction of $\overline{x}^*_{ij}$ as follows:

$$\overline{\overline{X}} = \overline{X}\cos\theta = \frac{\overline{x}_{ij}\overline{x}^*_{ij}}{\overline{X}^*} \tag{28}$$

$$\overline{\overline{\mathrm{d}X}} = \mathrm{d}\overline{X}\cos\theta = \frac{\mathrm{d}\overline{x}_{ij}\overline{x}^*_{ij}}{\overline{X}^*} \tag{29}$$

The concrete formulation of kinematic hardening model for anisotropic sand is described in another paper (Nakai and Funada, 1992).

The model for isotropic sand is extended to one for anisotropic sand only by introducing a fabric anisotropy tensor b_{ij} and modifying the stress ratio tensor x_{ij}. Now, for natural deposit sand, since two of the three principal values of b_{ij} are identical, i.e. $b_2 = b_3$, the tensor b_{ij} can be determined from the direction of deposition, the ratio of its principal values (b_1/b_3) and the condition of $b_{ii} = 3$.

5.2 Verification by Test Results

We will here analyse some kinds of element tests on anisotropic sands which are formulated by pouring sand in one direction, and discuss the validity of

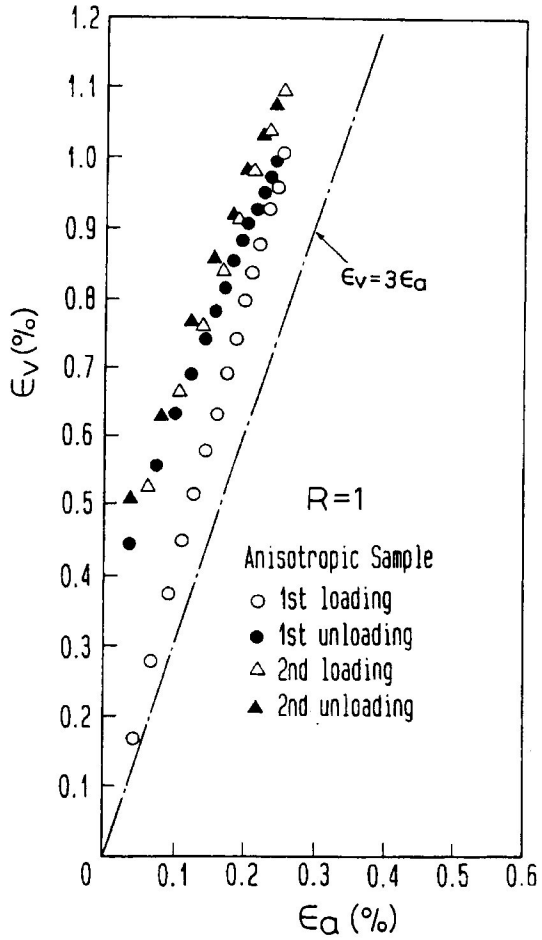

FIGURE 18. Experimental results of isotropic compression test on anisotropic sand ($\delta = 0°$)

the proposed model by comparing the analytical results with experimental data. In Fig. 17, the axes I_b, II_b and III_b imply the principal axes of b_{ij}, and $II_b - III_b$ plane is the bedding plane so that the principal values in II_b and III_b directions are identical ($b_2 = b_3$). The angle between the bedding plane and the major principal stress plane is equal to δ. The only parameter added in the model for anisotropic sand is the ratio b_1/b_3.

Figure 18 shows the results of isotropic compression test on anisotropic Toyoura sand whose bedding plane is horizontal ($\delta = 0°$), arranged in terms of axial strain ε_a and volumetric strain ε_v. It can be seen from the figure that the observed relation does not satisfy $\varepsilon_v = 3\varepsilon_a$ (dash-dotted line) under virgin loading because of inherent anisotropy, but the sand deforms isotropically under unloading and reloading ($d\varepsilon_v \approx 3d\varepsilon_a$). Such behaviour is described well by the proposed model as shown in Fig. 19.

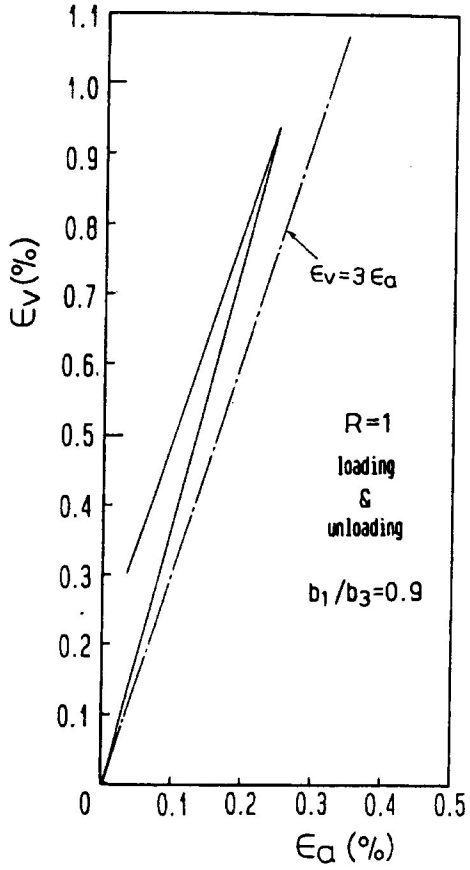

FIGURE 19. Analytical results of isotropic compression test on anisotropic sand ($\delta = 0°$)

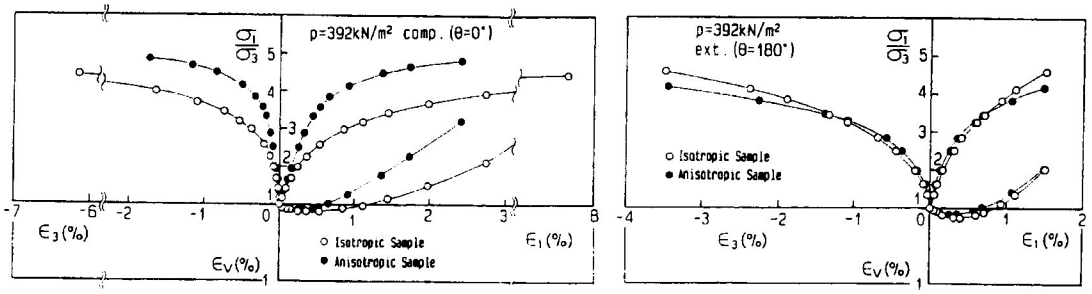

FIGURE 20. Experimental results of constant mean principal stress tests on isotropic and anisotropic sands, (a) triaxial compression, (b) triaxial extension

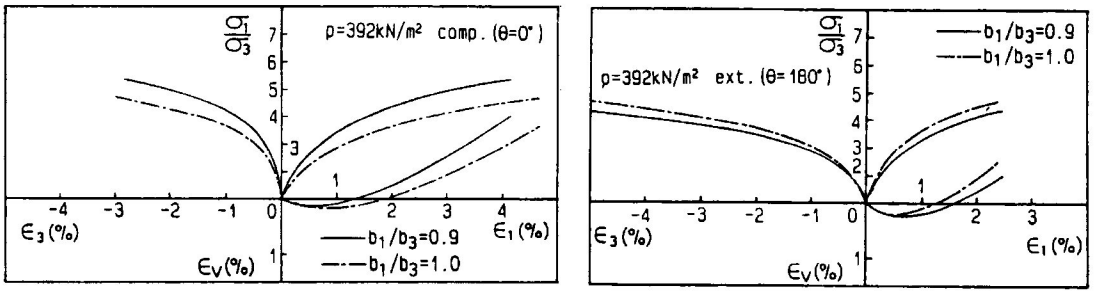

FIGURE 21. Analytical results of constant mean principal stress tests on isotropic and anisotropic sands, (a) triaxial compression, (b) triaxial extension

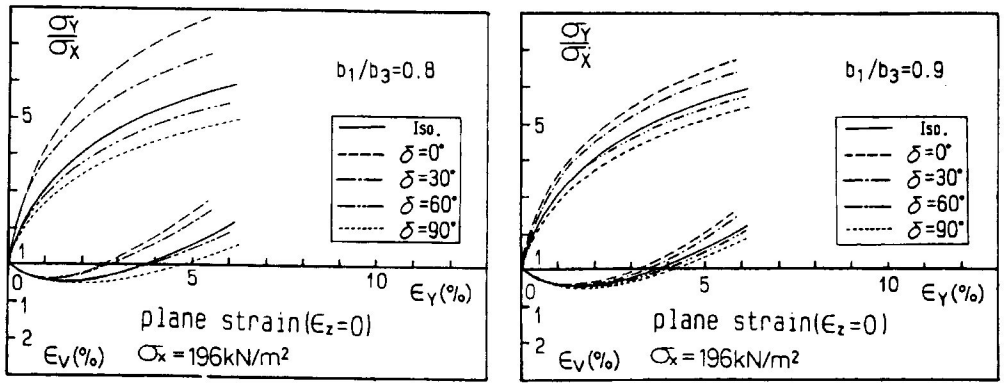

FIGURE 22. Calculated stress-strain relation in plane strain tests on anisotropic sand

Figure 20 shows results of mean principal stress tests on isotropic and anisotropic ($\delta = 0°$) Toyoura sand under triaxial compression and extension conditions. Figure 21 shows the analytical results corresponding to Fig. 20. In Fig. 21, the results of $b_1/b_3 = 1.0$ are for isotropic sample. The analytical results in Fig. 21 describe well the differences in deformation and strength characteristics for both isotropic sample and anisotropic sample.

Plane strain tests and triaxial compression tests were performed by Oda et al. (1978) on anisotropic Toyoura sand. Various angles δ (Fig. 17) between major principal stress plane and bedding plane were employed for sample preparation. Figure 22 shows the calculated stress-strain curves corresponding to the plane strain tests. The calculated relation between principal stress ratio $(\sigma_1/\sigma_3)_f$ and the angle δ is shown in Fig. 23 (figure (a): plane strain tests; figure (b): triaxial compression tests). The influence of the angle δ on the strength is also satisfactorily described by the model.

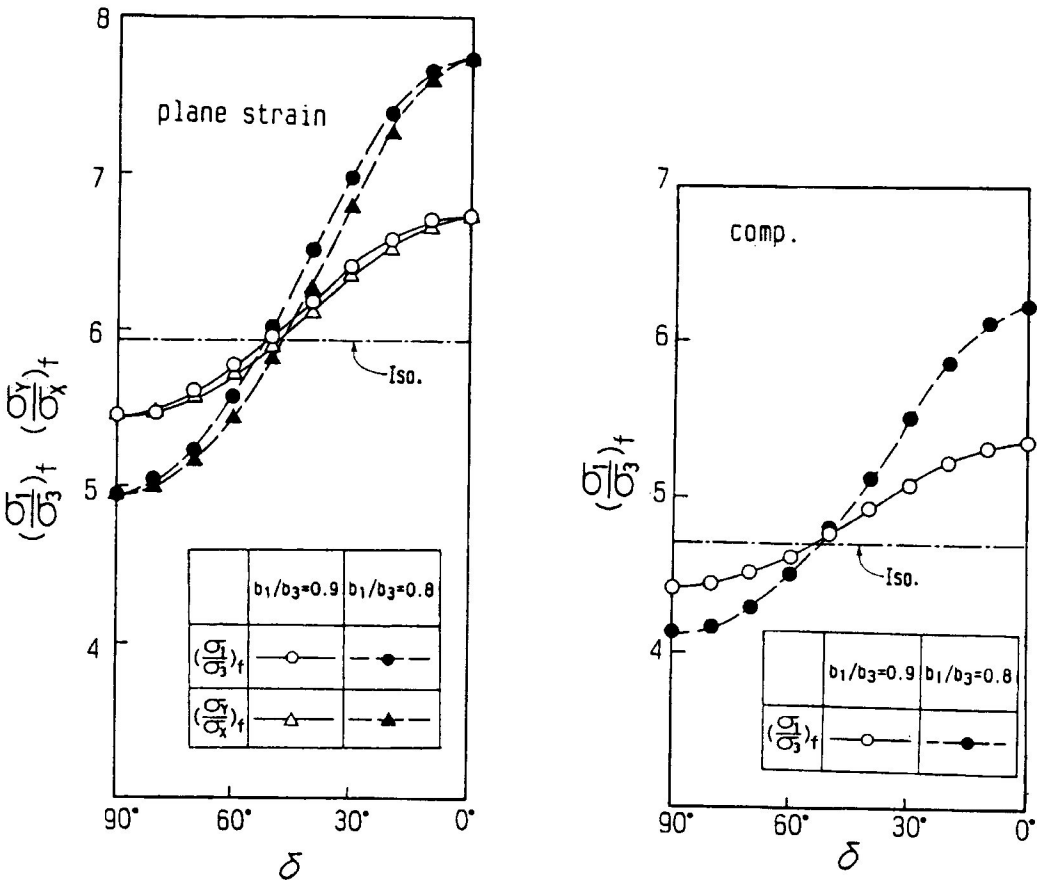

FIGURE 23. Calculated relation between stress ratio at failure and angle δ, (a) plane strain, (b) triaxial compression

6 Conclusions

(1) A modified stress tensor t_{ij} is presented to describe uniquely the deformation and strength characteristics of sand in three-dimensional stresses. The stress tensor t_{ij} is given by the inner product of the usual stress tensor σ_{ik} and the symmetric tensor a_{kj} whose principal values are the direction cosines of SMP. The influence of intermediate principal stress is properly taken into consideration in elastoplastic models by formulating the yield function and others using t_{ij} in place of σ_{ij} and by assuming the flow rule not in σ_{ij} space but in t_{ij} space.

(2) An isotropic hardening model for sand is formulated using the t_{ij}-concept. In the model, stress path dependency of the flow rule is taken into consideration by dividing the plastic strain increment into two components: the plastic component which satisfies the associated flow rule in t_{ij} space and the plastic component which represents

isotropic compression. This model can also describe positive and negative dilatancy by employing the plastic work W^{*p} based on t_{ij} as a strain hardening parameter.

(3) The isotropic hardening model is extended to a kinematic hardening model to take into consideration stress induced anisotropy in sand such as cyclic loading, rotation of principal stress axes and others. A kinematic hardening rule is assumed in the stress ratio tensor x_{ij} space so that the yield surface rotates about origin under shear loading and expands isotropically or anisotropically under proportional loading.

(4) The above model is extended to one which take into consideration inherent anisotropy as well. Only by modifying the stress ratio tensor x_{ij} with a fabric anisotropy tensor b_{ij}, the behaviour of sand with inherent anisotropy is naturally described.

7 References

Arthur, J. R. F. and A. Assadi (1977): Ruptured sand sheared in plane strain, *Proc. 9th ICSMFE*, **1**, 19-22.

Matsuoka, H. and T. Nakai (1974): Stress-deformation and strength characteristics of soil under three-different principal stresses, *Proc. JSCE*, **242**, 59-70.

Nakai, T. (1989): An isotropic hardening elastoplastic model for sand considering the stress path dependency in three-dimensional stresses, *Soils and Foundations*, **29**(1), 119-137.

Nakai, T., J. Fujii and H. Taki (1989): Kinematic extension of an isotropic hardening model for sand, *Proc. NUMOG III*, Niagara, 36-45.

Nakai, T. and T. Funada (1992): Elastoplastic modelling of soil anisotropy, *Proc. US-Japan Seminar on Micromechanics of Granular Materials*, Potsdam, 213-222.

Nakai, T. and H. Mihara (1984): A new mechanical quantity for soil and its application to elastoplastic constitutive model, *Soils and Foundations*, **24**(2), 82-94.

Oda, M., I. Koishikawa and T. Higuchi (1978): Experimental study on anisotropic shear strength of sand by plane strain test, *Soils and Foundations*, **18**(1),25-38.

Schofield, A. N. and C. P. Wroth (1968): Critical State Soil Mechanics, McGraw-Hill, London.

Sekiguchi, H. and H. Ohta (1977): Induced anisotropy and time dependency in clays, *Proc. Speciality Session 9*, 9th ICSMFE, Tokyo, 229-238.